



Using the Universal Atrial Coordinate System for MRI and Electroanatomic Data Registration in Patient-Specific Left Atrial Model Construction and Simulation

Marianne Beach, Iain Sim, Arihant Mehta, Irum Kotadia, Daniel O'Hare, John Whitaker, Jose Alonso Solis-Lemus, Orod Razeghi, Amedeo Chiribiri, Mark O'Neill, Steven Williams, Steven A. Niederer, and Caroline H. Roney^(✉)

Department of Biomedical Engineering, King's College London, London, UK
caroline.roney@kcl.ac.uk

Abstract. Current biophysical atrial models for investigating atrial fibrillation (AF) mechanisms and treatment approaches use imaging data to define patient-specific anatomy. Electrophysiology of the models can be calibrated using invasive electrical data collected using electroanatomic mapping (EAM) systems. However, these EAM data are typically only available after the catheter ablation procedure has begun, which makes it challenging to use personalised biophysical simulations for informing procedures. In this study, we first aimed to derive a mapping between LGE-MRI intensity and EAM conduction velocity (CV) for calibrating patient-specific left atrial electrophysiology models. Second, we investigated the functional effects of this calibration on simulated arrhythmia properties. To achieve this, we used the Universal Atrial Coordinate (UAC) system to register LGE-MRI and EAM meshes for ten patients. We then post-processed these data to investigate the relationship between LGE-MRI intensities and EAM CV. Mean atrial CV decreased from 0.81 ± 0.31 m/s to 0.58 ± 0.18 m/s as LGE-MRI image intensity ratio (IIR) increased from $IIR < 0.9$ to $1.6 \leq IIR$. The relationship between IIR and CV was used to calibrate conductivity for a cohort of 50 patient-specific models constructed from LGE-MRI data. This calibration increased the mean number of phase singularities during simulated arrhythmia from 2.67 ± 0.94 to 5.15 ± 2.60 .

Keywords: Atrial fibrillation · Patient-specific modelling · Atrial imaging · Registration · Conduction velocity

1 Introduction

Current biophysical atrial models for investigating atrial fibrillation (AF) mechanisms and treatment approaches typically use imaging data to define patient-specific anatomy [1]. These models may also include representations of fibrotic remodelling according to fibrosis distributions estimated from late-gadolinium enhancement magnetic resonance imaging (LGE-MRI) data [2]. Recent studies have demonstrated the importance of electrophysiology, including the conduction velocity (CV) of electrical propagation, on AF

mechanisms [3]. The electrophysiological properties of models can be calibrated using invasive electrical data from electroanatomic mapping (EAM) systems to construct personalised models [4]. However, these EAM data are typically only available after the catheter ablation procedure has begun, which makes it challenging to use personalised biophysical simulations for informing procedures.

Recent studies have identified a spatial correlation between the distribution of LGE-MRI intensities and CV. For example, Fukumoto et al. demonstrated reduced CV in regions of increased gadolinium uptake that may indicate regions of fibrosis [5]. In addition, Ali et al. showed that the degree of association between LGE-MRI intensity and CV depends on the measurement scale used for this analysis [6]. Caixal et al. demonstrated that areas with higher LGE exhibit lower voltage and slower CV in sinus rhythm [7]. While these studies show that spatial correlations between LGE-MRI and electrophysiological properties (including CV) can be identified, these relationships have not been used for calibrating cohorts of patient-specific models. Building personalised models by calibrating CV to LGE-MRI intensities means that patient-specific models can be constructed pre-procedure, using non-invasive data, and utilized to predict patient-specific treatment response. Furthermore, the functional implications of these relationships have not been fully investigated. For example, the effects of fibrosis derived changes in CV on arrhythmia mechanisms, including the number of stability of re-entries, are unknown [8].

In this study, first we aimed to derive a mapping between LGE-MRI intensity and EAM CV. Second, we aimed to investigate the functional effects of calibrating patient-specific models using this mapping on simulated arrhythmia properties. We previously developed a technique for registering atrial datasets: the Universal Atrial Coordinate (UAC) system [9]. We will use the UAC system to register LGE-MRI to EAM data, and to investigate the relationship between LGE-MRI intensities and EAM bipolar peak-to-peak voltage and CV. We will then use the measured relationship to calibrate conductivity across a cohort of patient-specific left atrial models constructed from LGE-MRI data. Finally, we will investigate the effects of conductivity personalisation on predicted arrhythmia dynamics.

2 Methodology

2.1 Data Modalities, Mesh Processing and Universal Atrial Coordinates

Personalised anatomical models were constructed from LGE-MRI data for ten patients undergoing first-time ablation at St Thomas' Hospital, UK. Seven of these patients had paroxysmal AF and 3 patients had persistent AF. MRI data included contrast-enhanced magnetic resonance angiogram (CE-MRA) scans and LGE-MRI data. The CE-MRA data was used to define the left atrial endocardial wall and the LGE-MRI data was used to estimate the patient-specific distribution of atrial fibrosis. Imaging data were obtained using previously described methods [10]. Ethical approval was given by both the local institutional review board (17/LO/0150; IRAS ID: 217417) and local research and ethics committee (15/LO/1803). Segmentation of CE-MRA data was performed semi-automatically [11] using CemrgApp software [12].

The process of constructing personalised anatomical models involves several steps, which are shown in Fig. 1. Initial meshes (see Fig. 1A), generated from either CE-MRA data segmentations or EAM data, were processed using Paraview. Artefacts were removed and then the data were refined using MeshLab. Filters were applied using Meshlab, including Poisson surface reconstruction, marching cubes and quadric collapse edge decimation (see Fig. 1B). The atrial meshes were then clipped at the pulmonary vein (PV) openings and the mitral valve (see Fig. 1C). Then each of the following structures were labelled using Paraview (see Fig. 1D): the right superior and inferior and left superior and inferior PVs, and the left atrial appendage (LAA).

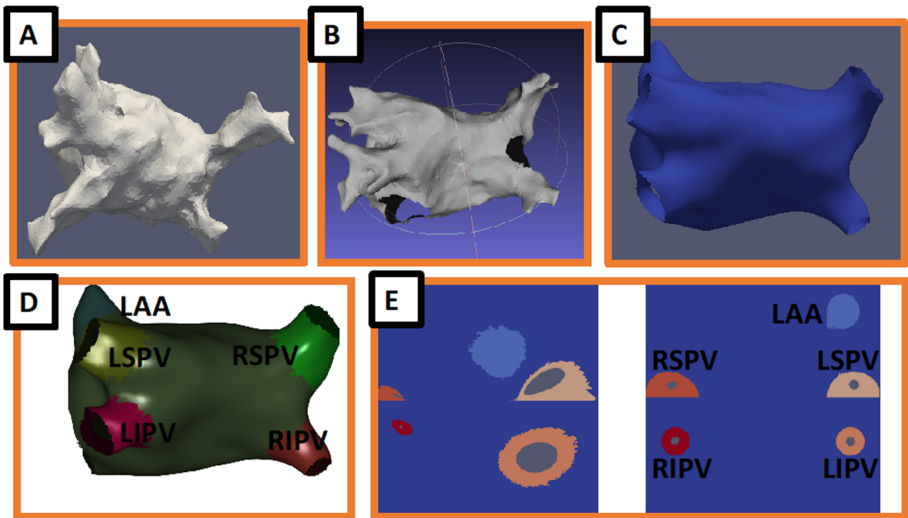


Fig. 1. The model construction process, including calculating Universal Atrial Coordinates from EAM/LGE-MRI surface meshes. (A) Input data (LGE-MRI or EAM). (B) Anatomical meshes refined using MeshLab filters. (C) Mitral valve opening and vessel clipping using Paraview. (D) Labelling of right superior and inferior and left superior and inferior pulmonary veins and left atrial appendage. (E) Conversion from 3D surface to 2D format, ready for further processing. Abbreviations: LSPV: left superior pulmonary vein, LIPV: left inferior pulmonary vein, RSPV: right superior pulmonary vein, RIPV: right inferior pulmonary vein, LAA: left atrial appendage

To calculate UAC, three landmarks were selected as follows: two on the roof at the junction of the left atrial body with the left superior and right superior PVs, and one on the septal wall at the fossa ovalis location. These landmarks were used to calculate geodesic paths used as boundary conditions for a series of Laplace solves. These boundary conditions fix the locations of the junctions of the LA body with each of four PVs and LAA to standard locations in the unit square (see Fig. 1E), using two coordinates: an anterior-posterior coordinate and a lateral-septal coordinate [9, 13]. The contours of the PV openings were also fixed to standard circles in UAC.

2.2 Calculating Conduction Velocity

EAM data exported from the Carto EAM system were read into Matlab using the OpenEP analysis platform (available open source at: openep.io [14]) and post-processed to estimate atrial CV. Local activation times (LATs) assigned by the Carto system were post-processed, together with the electrogram recording locations; see Fig. 2A for an example. For each electrogram recording location, the CV was estimated using the cosine-fit method [15]. Specifically, recording locations together with LATs within a 1 cm radius of the target electrogram recording location were fit to a planar wave and CV was estimated [16]. Locations with fewer than 5 points used for CV estimation were excluded. This calculation is demonstrated in Fig. 2B.

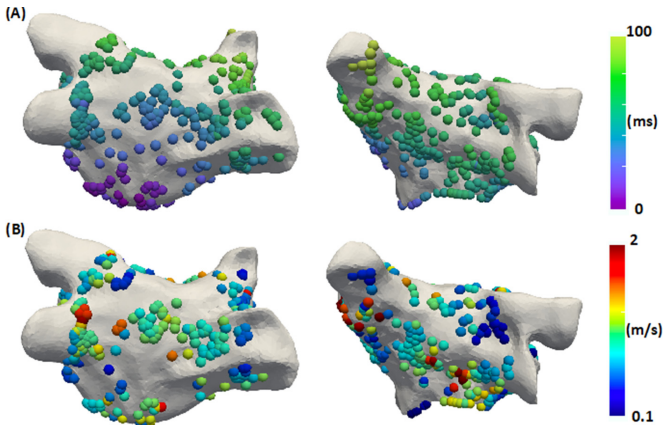


Fig. 2. Calculating electroanatomic mapping conduction velocity from local activation time maps. (A) Example local activation time (LAT) map and (B) example conduction velocity map.

2.3 Registering Imaging and Electrical Data

UAC were calculated as described in Sect. 2.1 for both LGE-MRI meshes and EAM meshes. Each electrode location, together with its CV and bipolar peak-to-peak voltage value, was mapped to UAC. These UAC locations were then mapped to the LGE-MRI mesh using the LGE-MRI UAC mapping. This enabled registration of the EAM data to the LGE-MRI mesh. For each EAM data point that was registered to the LGE-MRI mesh, the closest LGE-MRI node was located for analysis, and data were considered as paired LGE-MRI intensities with EAM measurements (bipolar peak-to-peak voltage and CV). This registration is demonstrated in Fig. 3.

2.4 Constructing an Average Atlas

To investigate the distribution of LGE-MRI intensities, CV and bipolar voltage across patients, we constructed average maps. All scalar fields were mapped to UAC and the average was calculated at UAC nodes corresponding to the first LGE-MRI mesh.

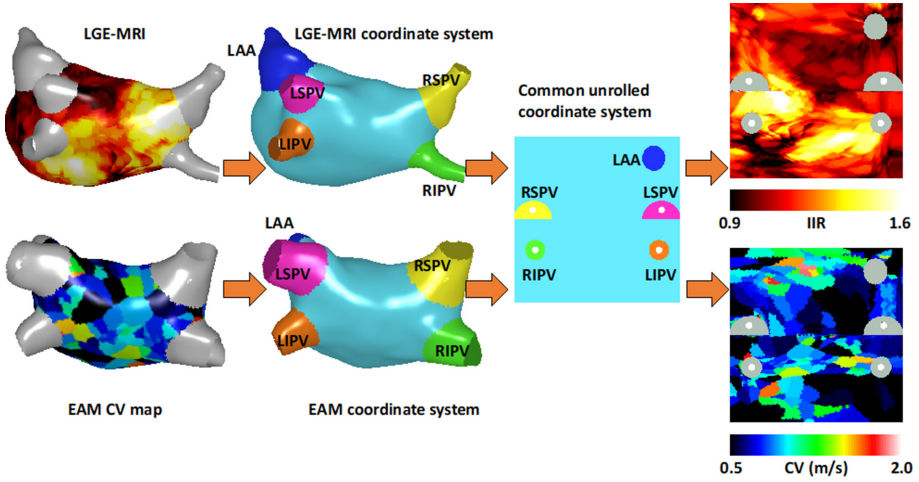


Fig. 3. Registration of LGE-MRI and electroanatomic mapping meshes using the Universal Atrial Coordinate system. Abbreviations: LSPV: left superior pulmonary vein, LIPV: left inferior pulmonary vein, RSPV: right superior pulmonary vein, RIPV: right inferior pulmonary vein, LAA: left atrial appendage, IIR: image intensity ratio, EAM: electroanatomic mapping, CV: conduction velocity.

2.5 Binning Electrical Data by LGE-MRI Intensity

To investigate the relationship between LGE-MRI intensity values, CV and bipolar peak-to-peak voltage, we first post-processed the LGE-MRI intensity field to calculate the image intensity ratio (IIR) by dividing the intensity field by the blood pool mean [17]. Each EAM electrode location was assigned to a bin depending on the LGE-MRI intensity value of its registered location on the MRI mesh. LGE-MRI intensity bins were as follows: $IIR < 0.9$ ('healthy'), $0.9 < IIR < 1.1$ ('mild fibrotic remodelling'), $1.1 < IIR < 1.4$ ('mild-moderate'), $1.4 < IIR < 1.6$ ('moderate-severe'), $1.6 < IIR$ ('severe'). For each bin, we considered CV and bipolar voltage values for each individual mesh, as well as for all meshes together.

2.6 Personalising Electrophysiology in Patient-Specific Models

We used a previously constructed cohort of 50 patient-specific bilayer left-atrial anatomies [2] with endocardial and epicardial fibre fields mapped to each anatomy from a DT-MRI dataset using UAC [13]. We calibrated each patient-specific model based on their LGE intensity map. Specifically, we assigned longitudinal conductivity values to LGE-MRI intensities within each of the bins depending on the average CV for that bin. The mapping used between CV and longitudinal conductivity was estimated for the Courtemanche et al. AF atrial cell model [18] by pacing in a 1D cable. Longitudinal conductivity was assigned following this mapping, and transverse conductivity was assigned to be the longitudinal conductivity divided by four, to give a homogeneous anisotropy ratio, following previous studies [19, 20]. In addition, ionic changes were included in

regions with $IIR > 1.22$ to include the effects of transforming growth factor- $\beta 1$: maximal ionic conductances were rescaled as 50% g_{K1} , 60% g_{Na} and 50% g_{CaL} [1, 21].

Simulations were performed using the Cardiac Arrhythmic Research Package software (available at opencarp.org [22]). For each anatomy, arrhythmia was induced using a technique that seeds phase singularities, as in our previous study [2]. Arrhythmia simulations were performed for anatomies with or without calibration. These simulations were post-processed to calculate phase singularity maps [21].

3 Results

3.1 Anatomical, Structural and Electrical Maps – Distributions of LGE-MRI Intensities, CV and Peak-to-Peak Bipolar Voltage

We analysed 7 paroxysmal patients and 3 persistent patients; see Table 1 for characteristics. Figure 4 A shows LGE-MRI distributions for each patient.

Table 1. Patient characteristics.

Age (years)	63.1 ± 9.8
Female	5
BMI	25.8 ± 2.7
Mean CHADS2 score	$1.8 (0-4)$
Mean LVEF (%)	62.8 ± 5.6
Hypertension	4

An area of increased intensity on the posterior wall close to the left inferior pulmonary vein was observed for all of the patients. Consequently, this area was also seen in the average LGE-MRI intensity map in Fig. 4B. Calculating the average map allows identification of any trends across patients. Benito et al. also observed a preferential distribution of increased LGE-MRI intensity close to the LIPV across a cohort of 113 patients [23]. The average CV distribution is shown in Fig. 4C and the average peak-to-peak bipolar voltage distribution in Fig. 4D. The mean CV calculated as a mean value across the left atrium for each case varied in the range: 0.69–1.00 m/s.

3.2 Binning Electrical Data by LGE-MRI Intensity

Table 2 gives the mean and standard deviation of the CV values and bipolar peak-to-peak voltage values for each of the LGE-MRI intensity bins. A decrease in mean peak-to-peak bipolar voltage was seen with increasing IIR, with a lower mean peak-to-peak bipolar voltage in the $1.4 \leq IIR < 1.6$ and $1.6 \leq IIR$ bins. Mean CV decreased when fibrosis IIR increased from $IIR < 0.9$ to $0.9 \leq IIR < 1.1$, and then further decreased for $IIR > 1.6$. Longitudinal conductivity values used for calibrating simulations are given for each IIR bin in the final column.

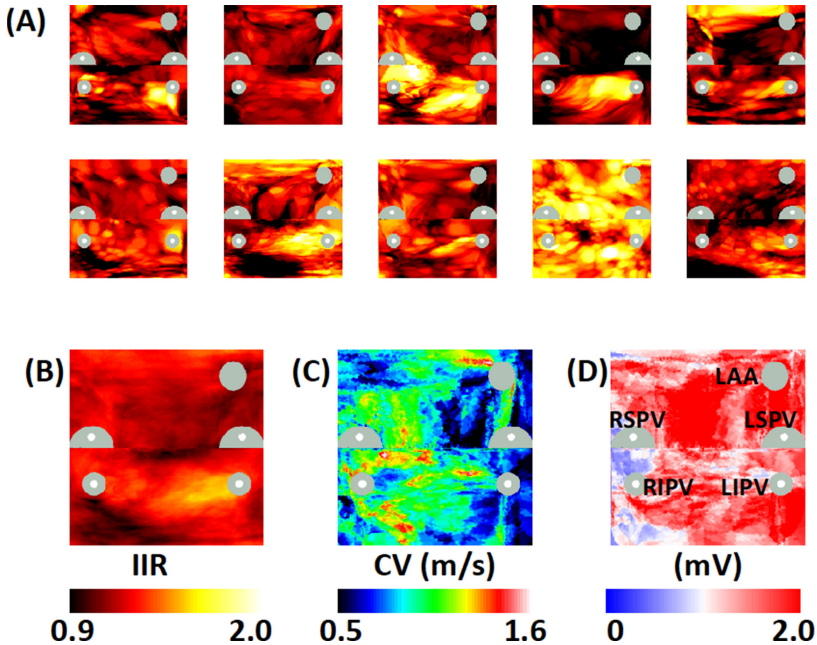


Fig. 4. Average distributions of LGE-MRI image intensity ratio, conduction velocity and peak-to-peak bipolar voltage. (A) Image intensity ratio (IIR) distributions displayed in UAC across the ten cases. (B) Average IIR map. (C) Average conduction velocity (CV) map. (D) Average peak-to-peak bipolar voltage map.

Table 2. LGE bins and mean conduction velocity and bipolar peak-to-peak voltage for each bin Values are given as mean and standard deviation.

LGE IIR	Bipolar voltage (mV)	CV (m/s)	Conductivity (S/m)
$\text{IIR} < 0.9$	1.29 ± 1.11	0.81 ± 0.31	0.4
$0.9 \leq \text{IIR} < 1.1$	1.42 ± 1.14	0.74 ± 0.32	0.31
$1.1 \leq \text{IIR} < 1.4$	1.13 ± 1.07	0.74 ± 0.32	0.31
$1.4 \leq \text{IIR} < 1.6$	0.72 ± 0.71	0.71 ± 0.30	0.28
$1.6 \leq \text{IIR}$	0.50 ± 0.35	0.58 ± 0.18	0.19

3.3 Patient-Specific Arrhythmia Simulations

Simulations without calibration had a longitudinal conductivity of 0.4S/m, and a transverse conductivity of 0.1S/m, equivalent to an average CV of 0.81 m/s. Calibrated simulations used these conductivity values for regions of $\text{IIR} < 0.9$, while for $\text{IIR} > 0.9$, longitudinal conductivities followed Table 2. Arrhythmia simulations were post-processed to compare properties such as the number of phase singularities. The mean number of phase singularities increased following calibration to LGE-MRI intensity values from

2.67 ± 0.94 for models without calibration to 5.15 ± 2.60 for models with calibration. This was significant with $p < 0.001$, paired t-test. The correlation between phase singularity maps calculated for models with and without calibration was low: 0.11 ± 0.14 (range: -0.06 – 0.76). This shows that patient-specific calibration has a large effect on predicted arrhythmia properties.

4 Discussion and Conclusions

Our methodology may be used for constructing personalised atrial models with patient-specific anatomy and conductivity from imaging and electrical data. We demonstrated that the measured relationship between LGE-MRI image intensity ratio and electroanatomic mapping CV can be used for calibrating atrial model CV in the case that only LGE-MRI data are available. This means that patient-specific models can be constructed using non-invasive data and utilized to predict patient-specific response to a range of treatment approaches before the patient undergoes a catheter ablation procedure.

The key limitation of our study is that it is a proof-of-concept study applied to ten patients only. Applying this methodology across a larger cohort of paroxysmal and of persistent patients is the subject of ongoing investigation, together with validation of the mapping. Image intensity ratio values may depend on the MRI scanner used. The choice of values used for binning IIR could be improved by comparing with expert visual assessment, or by choosing values to best separate populations of patients or types of tissue (e.g. healthy, pre-ablation fibrosis and post-ablation scar). Future work will determine the effects on the results of EAM recording resolution, MRI resolution and the choice of mesh used for calculating CV. In addition, recent inverse eikonal models that infer tissue anisotropy from EAM data [24] could be used for improved model calibration.

Acknowledgement. CR is funded by an MRC Skills Development Fellowship (MR/S015086/1). SN acknowledges support from the EPSRC (EP/M012492/1, NS/A000049/1, and EP/P01268X/1), the British Heart Foundation (PG/15/91/31812, PG/13/37/30280), and Kings Health Partners London National Institute for Health Research (NIHR) Biomedical Research Centre. SW acknowledges a British Heart Foundation Fellowship (FS 20/26/34952). This work was supported by the Wellcome/EPSC Centre for Medical Engineering (WT 203148/Z/16/Z).

References

1. Boyle, P.M., et al.: Computationally guided personalized targeted ablation of persistent atrial fibrillation. *Nat. Biomed. Eng.* **3**, 870–879 (2019). <https://doi.org/10.1038/s41551-019-0437-9>
2. Roney, C.H., et al.: In silico comparison of left atrial ablation techniques that target the anatomical, structural, and electrical substrates of atrial fibrillation. *Front. Physiol.* **11** (2020). <https://doi.org/10.3389/fphys.2020.572874>
3. Lalani, G.G., Schricker, A., Gibson, M., Rostamian, A., Krummen, D.E., Narayan, S.M.: Atrial conduction slows immediately before the onset of human atrial fibrillation: a bi-atrial contact mapping study of transitions to atrial fibrillation. *J. Am. Coll. Cardiol.* **59**, 595–606 (2012). <https://doi.org/10.1016/j.jacc.2011.10.879>

4. Corrado, C., Williams, S., Karim, R., Plank, G., O'Neill, M., Niederer, S.: A work flow to build and validate patient specific left atrium electrophysiology models from catheter measurements. *Med. Image Anal.* **47**, 153–163 (2018). <https://doi.org/10.1016/j.media.2018.04.005>
5. Fukumoto, K., et al.: Association of left atrial local conduction velocity with late gadolinium enhancement on cardiac magnetic resonance in patients with atrial fibrillation. *Circ. Arrhythmia Electrophysiol.* **9**, 1–7 (2016). <https://doi.org/10.1161/CIRCEP.115.002897>
6. Ali, R.L., et al.: Left atrial enhancement correlates with myocardial conduction velocity in patients with persistent atrial fibrillation. *Front. Physiol.* (2020). <https://doi.org/10.3389/fphys.2020.570203>
7. Caixal, G., et al.: Accuracy of left atrial fibrosis detection with cardiac magnetic resonance: correlation of late gadolinium enhancement with endocardial voltage and conduction velocity. *EP Eur.* **23**, 380–388 (2021). <https://doi.org/10.1093/europace/euaa313>
8. Haissaguerre, M., et al.: Intermittent drivers anchoring to structural heterogeneities as a major pathophysiological mechanism of human persistent atrial fibrillation. *J. Physiol.* **594**, 2387–2398 (2016). <https://doi.org/10.1113/JP270617>
9. Roney, C.H., et al.: Universal atrial coordinates applied to visualisation, registration and construction of patient specific meshes. *Med. Image Anal.* **55**, 65–75 (2019). <https://doi.org/10.1016/j.media.2019.04.004>
10. Sim, I., et al.: Reproducibility of Atrial Fibrosis Assessment Using CMR Imaging and an Open Source Platform. *JACC Cardiovasc. Imaging* **12**, 65–75 (2019). <https://doi.org/10.1016/j.jcmg.2019.03.027>
11. Sim, I., et al.: Reproducibility of atrial fibrosis assessment using CMR imaging and an open source platform. *JACC Cardiovasc. Imaging* **12**, 2076–2077 (2019). <https://doi.org/10.1016/j.jcmg.2019.03.027>
12. Razeghi, O., et al.: CemrgApp: an interactive medical imaging application with image processing, computer vision, and machine learning toolkits for cardiovascular research. *SoftwareX* **12**, (2020). <https://doi.org/10.1016/j.softx.2020.100570>
13. Roney, C.H., et al.: Constructing a human atrial fibre atlas. *Ann. Biomed. Eng.* (2020). <https://doi.org/10.1007/s10439-020-02525-w>
14. Williams, S.E., et al.: OpenEP: a cross-platform electroanatomic mapping data format and analysis platform for electrophysiology research. *Front. Physiol.* **88**, 105–121 (2021)
15. Roney, C.H., et al.: An automated algorithm for determining conduction velocity, wavefront direction and origin of focal cardiac arrhythmias using a multipolar catheter. In: 2014 36th Annual International Conference of the IEEE Engineering in Medicine and Biology Society, pp 1583–1586. IEEE (2014)
16. Roney, C.H., et al.: A technique for measuring anisotropy in atrial conduction to estimate conduction velocity and atrial fibre direction. *Comput. Biol. Med.* **104**, 278–290 (2019). <https://doi.org/10.1016/j.combiomed.2018.10.019>
17. Khurram, I.M., et al.: Magnetic resonance image intensity ratio, a normalized measure to enable interpatient comparability of left atrial fibrosis. *Hear Rhythm* **11**, 85–92 (2014). <https://doi.org/10.1016/j.hrthm.2013.10.007>
18. Courtemanche, M., Ramirez, R.J., Nattel, S.: Ionic targets for drug therapy and atrial fibrillation-induced electrical remodeling: insights from a mathematical model. *Cardiovasc. Res.* **42**, 477–489 (1999)
19. Bayer, J.D., Roney, C.H., Pashaei, A., Jaïs, P., Vigmond, E.J.: Novel radiofrequency ablation strategies for terminating atrial fibrillation in the left atrium: a simulation study. *Front. Physiol.* **7**, 108 (2016). <https://doi.org/10.3389/fphys.2016.00108>
20. Roney, C.H., et al.: A technique for measuring anisotropy in atrial conduction to estimate conduction velocity and atrial fibre direction. *Comput. Biol. Med.* **104**, 278–290 (2019). <https://doi.org/10.1016/j.combiomed.2018.10.019>

21. Roney, C.H., et al.: Modelling methodology of atrial fibrosis affects rotor dynamics and electrograms. *Europace* (2016). <https://doi.org/10.1093/europace/euw365>
22. Plank, G., et al.: The openCARP Simulation Environment for Cardiac Electrophysiology. *bioRxiv*, 1–22 (2021). <https://doi.org/10.1101/2021.03.01.433036>
23. Benito, E.M., et al.: Preferential regional distribution of atrial fibrosis in posterior wall around left inferior pulmonary vein as identified by late gadolinium enhancement cardiac magnetic resonance in patients with atrial fibrillation. *Europace* **20**, 1959–1965 (2018). <https://doi.org/10.1093/europace/euy095>
24. Grandits, T., Pezzuto, S., Lubrecht, Jolijn M., Pock, T., Plank, G., Krause, R.: PIEMAP: Personalized Inverse Eikonal Model from Cardiac Electro-Anatomical Maps. In: Puyol Anton, E., Pop, M., Sermesant, M., Campello, V., Lalande, A., Lekadir, K., Suinesiaputra, A., Camara, O., Young, A. (eds.) STACOM 2020. LNCS, vol. 12592, pp. 76–86. Springer, Cham (2021). https://doi.org/10.1007/978-3-030-68107-4_8